Graphical Abstract:

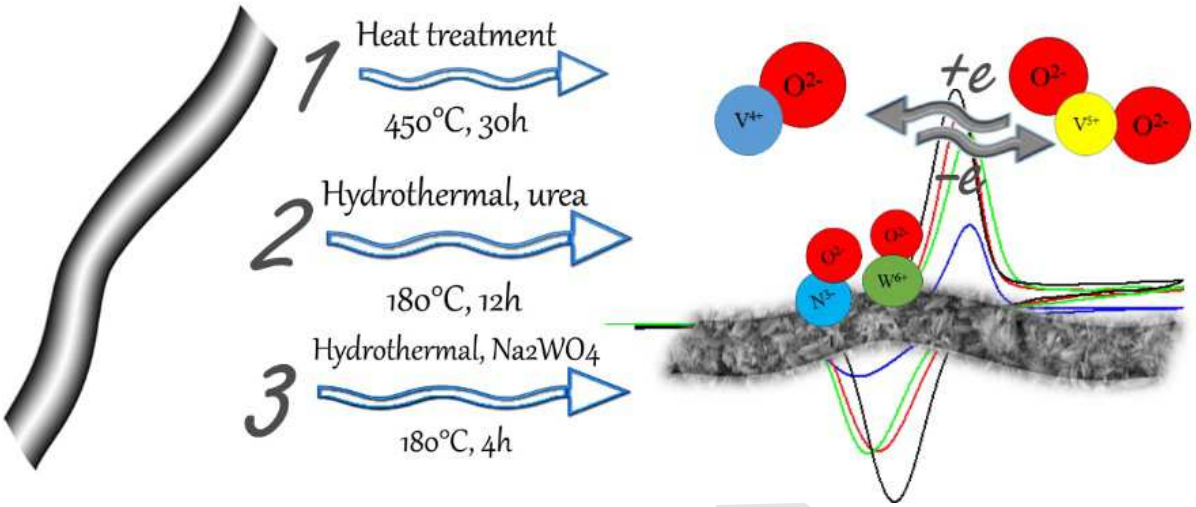

High-power positive electrode based on synergistic effect of N- and WO_3 decorated carbon felt for vanadium redox flow batteries

Mir Ghasem Hosseini [a, b*1], Seyedabolfazl Mousavihashemi [a, c], Sebastián Murcia-López[c], Cristina Flox [c*2], Teresa Andreu [c], Joan Ramón Morante [c, d]

[a] Department of Physical Chemistry, Electrochemistry Research Laboratory, University of Tabriz, Tabriz, Iran

[b] Engineering Faculty, Department of Materials Science and Nanotechnology, Near East University, 99138, Nicosia, North Cyprus, Mersin 10, Turkey

[c] IREC, Catalonia Institute for Energy Research, Jardins de les Dones de Negre 1, Sant Adrià de Besós, 08930 (Spain)

Facultat de Física, Universitat de Barcelona, C. Martí i Franqués, 1, 08028, Barcelona, Spain

[1] * Corresponding author. Tel: +98 413 339 3138. E-mail: mg-hosseini@tabrizu.ac.ir (Mir Ghasem Hosseini)
[2] * Corresponding author. Tel: +34 933 562 615. E-mail: cflox@irec.cat (Cristina Flox)

Abstract

Although Vanadium Redox Flow Battery (VRFB) is well suitable for grid-scale application, their power-related cost must be reduced in order to boost the technology to the market, allowing their widespread commercialization. One effective way to make the VRFB a competitive and viable solution could be through the new strategies for improving the electrocatalytic activity of the electrodes with enhanced electrolyte/electrode interface characteristics. The greatly effective and enhanced-electron transfer could increase the current density with the decrement of the stack size. Herein, we report the synergistic effect demonstrated by N- and WO_3- decorated carbon-based positive electrode, named HTNW electrode, which demonstrates the feasibility of achieving: i) enhanced electrocatalytic activity, indicating high rate towards VO^{2+}/VO_2^{+} couple (promotion of oxygen and electron transfer processes), ii) decrement of the electron-transfer resistance from 75.62 Ω to 12.4 Ω for the pristine electrode and HTNW electrodes, respectively; iii) 51% of the electrolyte utilization ratio at high rates (i.e. 200 mA cm^{-2}) with 70% of energy efficiency ; iv) increment of more than 50% of the power–peak in comparison with HT electrode.

1. Introduction

Vanadium redox flow batteries (VRFB) are considered a prominent alternative to large-scale energy storage because of their outstanding features compared to other energy storage technologies (i.e. Lithium ion batteries) such as longer lifetime (10000 cycles), flexible design, and minimum self-discharge. However, despite of their maturity, cost reduction is the major challenge to overcome in order to achieve VRFB widespread application, including renewable integration, smart grid uses and off-grid electrification areas. This is mainly because the currently power-related cost is still too high, (state-of the art in VRFB €600/kW) and the existing alternatives present low roundtrip electrochemical energy efficiency at high-rates.

The power output is determined by size of the stacks through the number of cells and the active area of the electrodes. The stack components (i.e. proton exchange membrane and electrodes) directly define the performance of VRFB (e.g. high rate capability and long-term stability) since they establish the polarization and the ohmic resistance. In particular, the electrodes must facilitate the electron transfer process towards the positive and negative half-cell reactions (1, 2). Consequently, by enhancing the electrochemical properties of the electrodes the power density (i.e. current) can be increased, leading to a reduced stack size, and, as a consequence, decreasing the power-related cost (SET plan targets for batteries towards 2030 in EU €300/kW [1]).

$$VO_2^+ + 2H^+ + e^- \rightleftharpoons VO^{2+} + H_2O \qquad E°=1.0\ V \quad (1)$$

$$V^{3+} + e^- \rightleftharpoons V^{2+} \qquad E°= -0.26\ V \quad (2)$$

According to these reactions, the positive half-cell reaction (reaction 1) involves a kinetics that requires the contribution of protons, the interchange of an oxygen atom and an electron transfer process. The negative half-cell reaction involves only an electron transfer process (reaction 2). Thus, the kinetics of the VO^{2+}/VO_2^+ reactions becomes limited by the availability of O-containing groups (i.e. number of active sites) that enhance this oxygen interchange. Therefore, apart from the amount of oxygen functional groups (C=O, C-OH) on the surface, other features related to the electrode activity, such as wettability and adsorption of vanadium onto surface electrode become also decisive. It is worth mentioning that the formation of Carbon- Nitrogen-Vanadium intermediate especially via quaternary and/or oxidic nitrogen groups [4] is a key step for the enhancement of the electrocatalytic activity [2, 3], facilitating the electron transfer in the electrode/electrolyte interface

Intensive efforts have been made to improve the electrochemical activity of the carbon felts (CF) as positive electrodes by enhancing the surface area and/or the electrical conductivity by means of introducing several electrocatalysts. For example, MWCNTs [5], graphene nanosheets and carbon nanofibers [6, 7], functionalization of carbon surface as N-and O-containing groups [8], metals such as Pt [6], Ir [9] and Bi [10] and metal oxides Mn_3O_4[11, 12], WO_3[13, 14], TiO_2[15], CeO_2[16], PbO_2[17], and Nb_2O_5 [18] were deposited onto the CF supports to prepare modified electrodes. However, although all this research demonstrated an improvement in electrochemical kinetics, the enhanced power density is rarely discussed in the literature as a complementary performance evaluation to the charge/discharge experiments. Recently, significant work has been done by Mayrhuber et al. to increase the power density by means of improving the mass-transport losses in carbon paper electrode, achieving an increment in power density of 30% using perforated electrodes in comparison with pristine carbon paper electrode [19]. In parallel, Liu et al. demonstrated an increment in power density values of 16% using no-gap cell and air-treated electrodes [20]. Despite this relevant research devoted to (1) improving the surface area with functionalized electrodes, (2) enhancing mass-transport process and (3) designing novel VRFB prototypes using no-gap architectures, the improvement of the power density output of VRFB systems is still a major drawback preventing the cost from decreasing further.

In order to fill this gap and motivated by the idea to promote active sites for the adsorption of vanadium ions and enhancements in the electron and oxygen transfer processes, our strategy was based on the modification of the surface of carbon felt with the functionalization of N- and WO_3- containing groups. The performance of the VRFB has been evaluated as the combined effect of the aforementioned functionalities for their advantages such as low cost, easy preparation and high stability in sulfuric media in comparison with other metal oxides as IrO_3 or RuO_2. In this study, we used a hydrothermal process with urea and $Na_2WO_4 \cdot 2H_2O$ precursors as an efficient methodology to produce stable and large amounts of N- and O-functionalities. Moreover, the hydrothermal process is an environmentally friendly technology, very suitable for large-scale production.

It is worth mentioning that the WO_3-based electrodes have been extensively studied in the literature as electrocatalysts for VRFB. However, the discussion is limited to fundamental studies in three-electrode cell (Interlaced WO_3-carbon nanotube nanocomposite electrodeposited on graphite as a positive electrode in vanadium redox flow battery) or their application in a flow cell with a very low current density (ca. 50 $mAcm^{-2}$) [13]. Recently,

Kabtamu et al. studied the rate capability of WO_3-based electrodes in VRFB up to 160 mA cm^{-2}, obtaining a very low electrolyte utilization ratio (i.e. 16 %) using WO_3-based nanowire electrodes [18].

2. Experimental

2. 1 Synthesis of the as-prepared electrodes

Materials: Rayon-based carbon Felt (CF) with 6 mm of thickness was purchased from Societe Carbon-Lorraine. Urea with a quality BioReagent grade, sodium tungstate di-hydrate (≥99.0%) and vanadium oxide sulphate (≥99.9%) were obtained from Sigma–Aldrich, while sulphuric acid (95-98%), Chloridric acid (37%), oxalic acid (98%) were obtained from Labkem. All materials were used as received without further purification. Figure 1 shows a schematic representation of the synthesis process for the functionalization of the all electrodes. Firstly, all as-prepared electrodes of CF were thermally activated at 450°C for 30 hours in oxygen atmosphere in order to remove impurities, denoted as HT electrode.

Consequently, HT electrode was modified by introducing N-functionalities, using a simple and low-cost hydrothermal method. In this method, CF electrode was immersed in 80 mL solution of 4 M urea in deionized water. Next, it was put into an ultrasonic bath for 30 minutes, allowing the penetration of the solution into the electrode and then it was poured into a Teflon-lined autoclave reactor and the temperature was set to 180°C for 12 hours. After that, the reactor was cooled down to room temperature and the sample was taken out and washed with deionized water [21]. This electrode was labelled as HTN. The incorporation of WO_3-functionalities onto the surface of HT electrode was performed using 80 mL of precursor solution based on 0.05 M of $Na_2WO_4 \cdot 2H_2O$ salt in 2M HCl acidic media. The final pH was adjusted to 2.4 by oxalic acid. A homogeneous solution was obtained after stirring for 30 minutes. After that, the HT electrode was immersed in the solution and sonicated for 30 minutes. Finally, the hydrothermal reaction at 180°C with a duration of 3 hours was carried out. After cooling down to room temperature, the felt was washed many times to remove unattached WO_3 particles [14]. This sample was labelled as HTW electrode. The preparation of N and WO_3 co-modified CF was carried out using the same hydrothermal process applied to the HTN electrode. Finally, this electrode material was washed many times and dried at 60°C. This electrode was labelled as HTNW.

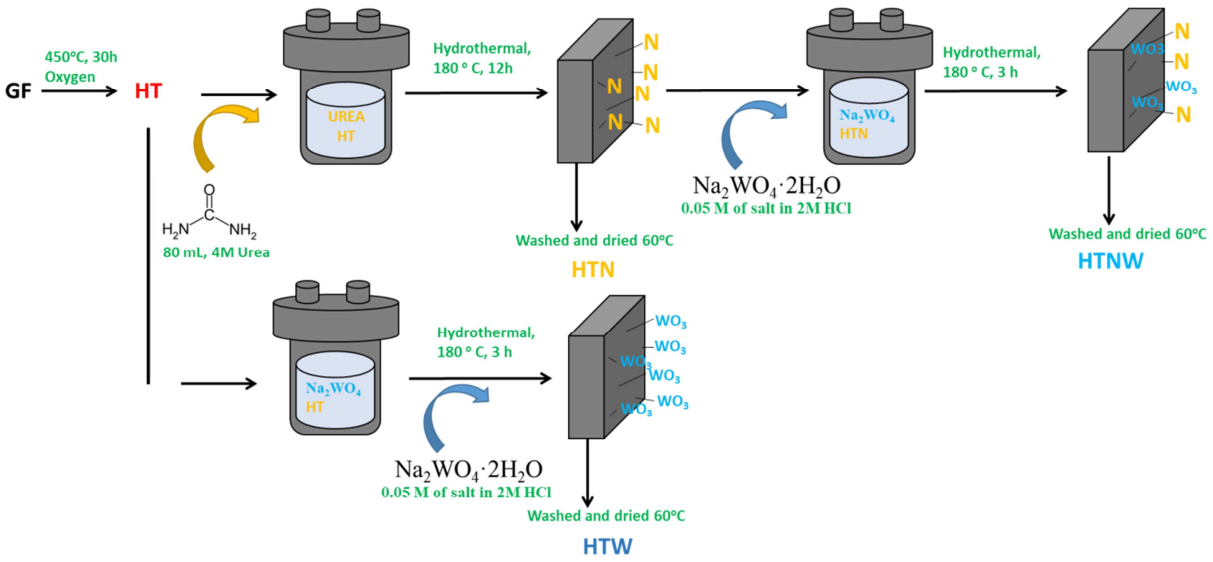

Figure 1. Illustration of the electrode preparation.

2. 2 Materials characterization

The morphology of prepared felt electrodes was examined by FE-SEM (using a field emission Zeiss Auriga® series instrument) with an accelerating voltage of 15 kV. The elemental composition of felt samples was investigated by energy dispersive X-ray spectroscopy (EDS) coupled with the SEM. The tungsten oxide crystal structure characterization was measured in a Bruker D8 Advance diffractometer equipped with a Cu Kα (1.54051 Å) radiation source. Bruker-Alpha FT-IR spectrophotometer in attenuated total reflection (ATR) configuration was used to obtain ATR-FTIR spectrum of all as-prepared felts in range of 375-4000 cm^{-1} with a resolution of 4 cm^{-1} and 24 scans. Dispersive spectrometer Jobin-Yvon Lab Ram HR 800 with Olympus BXFM microscope optic was used to obtain Raman spectra. The detector used was a CCD cooled to -70°C. Laser power on samples was 0.5 mW. The chemical composition changes of the surface of the HTNW electrode were analyzed by X-ray photoelectron spectroscopy (XPS) using a PHI instrument model 5773 Multi-technique with A1 Kα radiation (1486.6 eV).

2. 3 Electrochemical tests

The electrochemical activity of prepared samples was investigated with a cyclic voltammetry (CV) and electrochemical impedance spectroscopy (EIS). A piece of disk-shaped felt sample (Diameter 8mm, thickness 6mm) was connected to a platinum wire and served as working electrode. Hg/Hg_2SO_4/Sat. K_2SO_4 (0.664 V vs. SHE) and large surface area platinum mesh were used as reference and counter electrodes, respectively. 0.05 M $VOSO_4$ solution in 1 M

H_2SO_4 was used as three-electrode cell tests electrolyte. Different scan rates of 1 to 10 mV/s were applied in CV tests to obtain voltammetry diagrams for VO_2^+/VO^{2+} redox couple to investigate the diffusion reaction rates of different felt samples. EIS tests were studied by applying alternating voltage of 10mV over frequency range of 100kHz to 10mHz at open circuit potential (OCP). A Biologic® VMP-3 multi-channel potentiostat controlled by EC-lab® software was used to perform electrochemical tests.

2. 4 Single-cell performance

The single-cell performance of as-prepared electrodes was evaluated in the VRFB cell, using geometric area of electrodes of $3cm^2$ (i.e. positive electrode was as-prepared electrodes and negative electrode: HT) with a Nafion 117 membrane between positive and negative electrodes. 1.8 M $VOSO_4$ in 3M H_2SO_4 electrolyte was used as starting electrolyte for electrogeneration of other vanadium oxidation states as previously reported. The negative electrolyte tank was bubbled with nitrogen gas for the duration of the experiment for oxygen elimination. The flow rate of pumping positive and negative electrolytes into the cell was 30mL/min. The charge and discharge experiments were performed between 0.7 and 1.8 V in galvanostatic mode at $200mAcm^{-2}$. A schematic view of the used single cell is presented in Figure 2. Charge and discharge profiles (cell potential vs. capacity) were used to obtain electrolyte utilization ratio. A theoretical capacity of 965 mAh was calculated for 20 ml electrolyte in each compartment. In order to identify the mechanism of the voltage losses and the output of the voltage at specified current density, polarization curves were conducted using current-steady steps. In all cases, the discharging polarization curve started with the battery and, after that, the battery was discharged at the specified current density in the range of 0 to 500 $mAcm^{-2}$ for 30s, obtaining the output voltage. Finally, a rest period of 2 minutes to a steady state at OCP was applied. The power density curves were obtained from the product of output voltage and the corresponding current density.

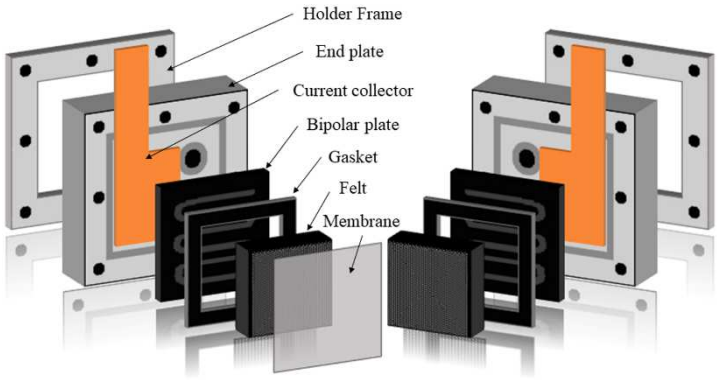

Figure 2. Schematic view of single cell used in electrochemical tests.

3. Results and discussion

3. 1 Surface characterization of as-prepared electrodes

The FE-SEM images of as-prepared samples are shown in Figure 3. As can be seen from the images, HT electrode consists of cross-linked carbon fibers. Thermal activation treatment of the felts smoothes and cleans the surface of HT electrode which is related to the removal of organic impurities [22] (Figure 3a). The average diameter of the carbon fibers in felt electrode was 15 µm. A visible difference can be observed in the morphology of HTN electrode relative to that of the bare CF electrode or that of the heat-treated HT electrode. Figure 3b shows the poor modification of the HTN electrode surface in comparison with the starting HT electrode, caused by the hydrothermal treatment with Urea. Comparing HTN and HTW electrodes in Figure 3c, we can observe that WO_3-functional groups have grown on the surface of the HT in an uneven distribution with a thickness layer of 1 µm (see FE-SEM cross-section in Figure S1), affecting to the morphology of the electrode. Higher magnification (Figure 3c) corroborated the morphology, which consists of several agglomerated structures that are primarily composed of nanorods. Due to the increase of hydrophilicity of the HTN electrode (Figure 3d), the coverage of WO_3 was more compact and homogenous, leading to the layer thickness increasing up to ca. 2 µm (see Figure S1). This indicates that the WO_3-functionalities can be easily prepared on the surface of the HTN electrode in comparison with HT electrode because of the improved wettability of the HTN electrode. Besides, WO_3-decoration does not affect the distribution of the carbon fibers of HTN.

EDS analysis corroborates the hypothesis that O- and N- functional groups are successfully introduced onto the surface of HT electrode by hydrothermal process, playing an important

role in the hydrophilicity of the electrode. EDS reveals that only C (100%) is found for HT sample (table S1). The surface rich in Nitrogen (21%) and Oxygen (10%) is found in the HTN samples because of the hydrothermal treatment with urea. However, a more enriched surface of Oxygen (60%) is obtained in the HTW electrode due to the presence of WO_3 on the surface. A combination of Nitrogen (5%) and Oxygen (66%) functionalities can be found in the HTNW electrode due to the hydrothermal treatment with WO_3 precursor on the HTN electrode. Note that a similar W content can be found in both electrodes, HTW and HTNW.

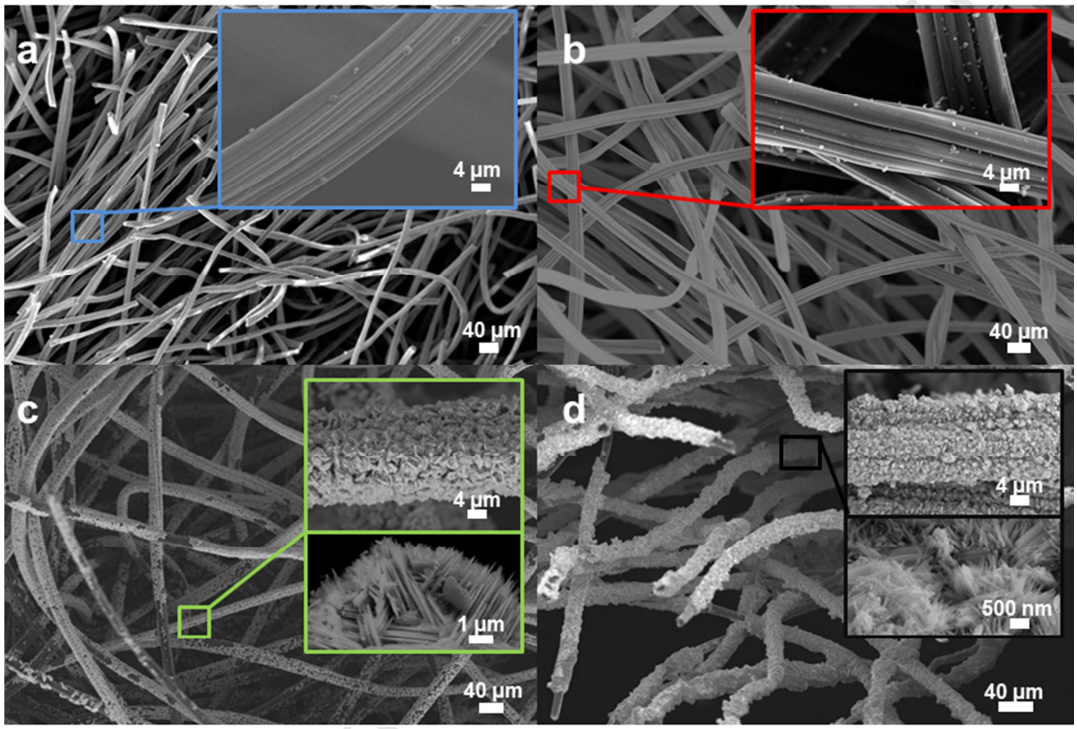

Figure 3 Morphologies of carbon felt electrodes after various surface modifications, a) thermal treatment: HT, b) Hydrothermal with urea: HTN, c) Hydrothermal with $Na_2WO_4 \cdot 2H_2O$: HTW and d) Hydrothermal with urea and $Na_2WO_4 \cdot 2H_2O$: HTNW electrodes.

X-ray diffraction pattern of as-prepared electrodes are given in Figure 4a. The broad peaks near 2θ = 25º and 43º in the spectrum of HT and HTN electrodes are attributed to the crystallographic planes of (002) and (004) of the originally CF electrode. Additional peaks at 13.9°, 22.8° and 27.9° are found in the HTW electrodes, which is consistent with the hexagonal WO_3 (100), (001) and (200) crystalline planes, respectively, which correspond to typical hexagonal WO_3 phase (JCPDS 00-033-1387) [14]. The lattice parameters were carefully estimated as a = b = 7.2980 and c = 3.8990. It is noteworthy that the patterns found for HTNW electrode are similar than that of HTW. However, the HTNW pattern shows a decrement of intensity in the peak 2θ around 25 degrees, which is characteristic of the

graphitic plate, also observed in the HTN electrode. The lattice obtained pattern for HTNW revealed that the N-functionalities incorporate in the surface cause lattice distortion and, in consequence, induce more defects.

For further inspection of the surface chemistry of the as-prepared CF electrodes, Fourier-transform infrared spectroscopy (FT-IR) was performed. As clearly shown in the Figure 4b, no significant peaks have been found in the HT electrode. However, several characteristic peaks at 1150, 1588, 1678 and 3425 cm^{-1}, appears in the sample HTN, corresponding to C-N-H bending, NH_2 scissoring, C=N bonding, and –NH, -NH_2 stretching , respectively [23]. It is a noteworthy that a strong band attributed to the presence of W-O-W bonds (stretching vibration) is observed as a wide and sharp peak at ca. υ= 600 cm^{-1}, in the HTW and HTNW electrodes. Inside of this wide peak, can be differenced two peaks, which is attributed to two different crystallinity of tungsten oxide in sample[24]. All samples show a weak peak at 3745 cm^{-1} as an indicator for hydroxide groups.

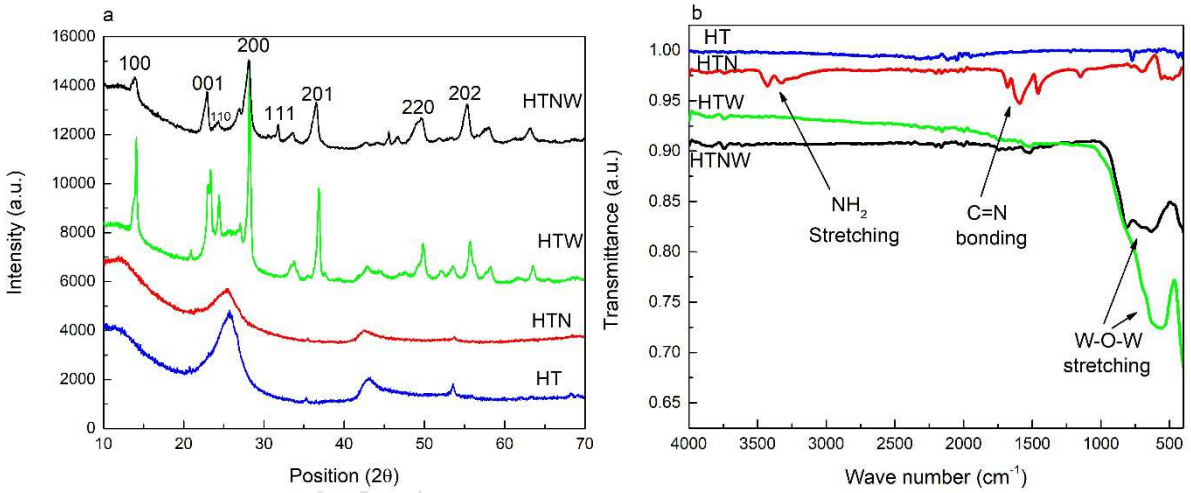

Figure 4. a) XRD pattern, b) ATR-FTIR spectra for as-prepared carbon felt samples

The structural changes in the graphitic structure of as–prepared were characterized by Raman spectroscopy, as shown in Figure 5. Two well-defined peaks are clearly appreciated at Raman shifts of 1350 cm^{-1} and 1580 cm^{-1}, attributed to sp^3 carbon bonds (D-band) and the carbon sp^2 bonds (G-band), respectively. From the collected Raman spectra, the ratio of the intensities (I_D/I_G) can be estimated, indicating the structure of the carbon defects of the electrodes prepared. [25]. The intensity ratio of the HTNW electrode (I_D/I_G = 1.19); HTW electrode (I_D/I_G = 1.25) and the HTN electrode (I_D/I_G = 1.37) are almost the same and, surprisingly, highly superior to HT electrode (I_D/I_G = 0.19). This indicates that the implementation of nitrogen and WO_3 functionalities process contributes to increasing the I_D/I_G ratio, suggesting

that the hydrothermal treatment causes a great increase of defective sites. No significant difference in the ID/IG ratio, which is constant and ca. 1.2 (see Figure S2), can be appreciated in the Raman spectra over the WO_3-related peaks in comparison with the CF-related peaks in the HTW electrode.

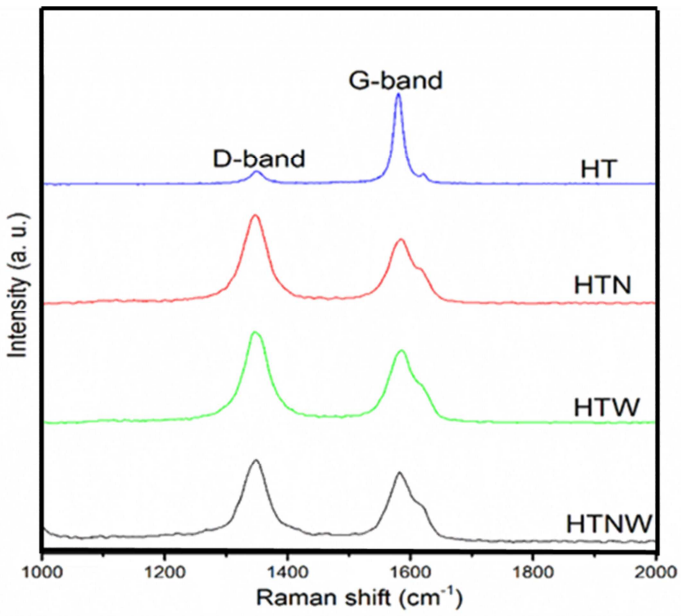

Figure 5. Raman spectra of the HT, HTN, HTW and HTNW electrodes

These results show that the HTNW electrode combines both, N and WO_3-functionalities, which have been successfully introduced on the surface on the CF. To complementary investigate the chemical environment of Nitrogen on the surface structure of the HTN and HTNW electrodes, Figure 6 shows the N binding energies from XPS analysis. The high-resolution of the N 1s region shows the following contributions: 1) nitrogen atoms in the pyridinic N-C groups (398.5 eV, N1); pyrrolic-N-C groups (399.8 eV, N2), quaternary N-C groups (401.0 eV; N3), and pyridine-N-O-groups (402.5 eV, N4) [26, 27].

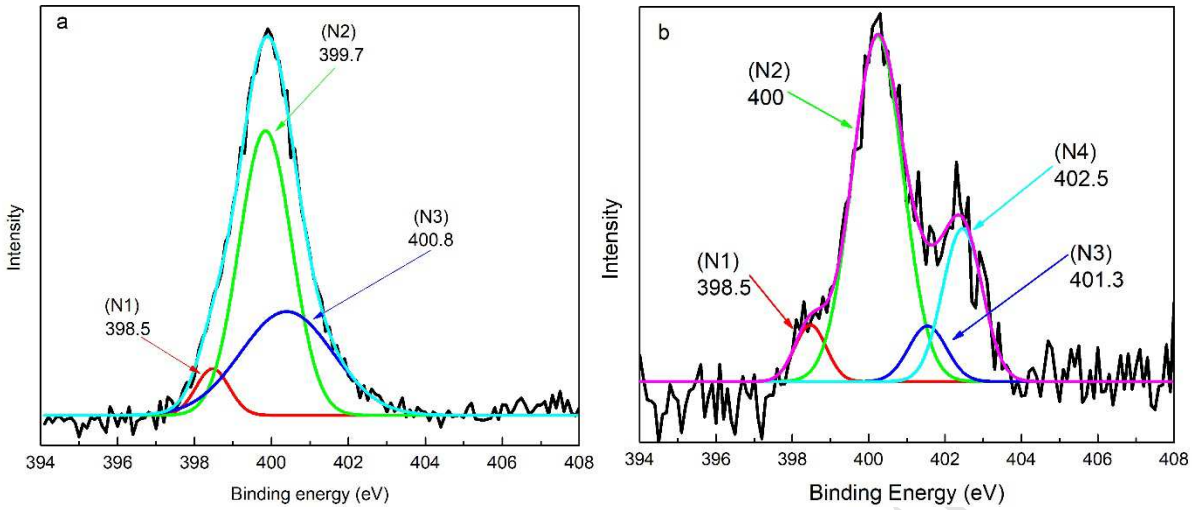

Figure 6. XPS survey for N1s spectra for; a) HTN, b) HTNW electrodes (N1: Pyridinic, N2: Pyrollic, N3: Quaternary, N4: Oxicidic).

Notably, the presence of the Pyridine-N-O-groups in the HTNW electrode related to the ambient undergone the sample during the WO_3 deposition the HTNW (Figure 6b). These functionalities could promote the synergistic effect, based on the following assumptions: i) The N-functionalities modify surface of the electrode in terms of wettability and thereby, alters the chemisorption characteristics of the vanadium ions, together with WO_3-functionalities; ii) Incorporation of highly content of active sites in order to overcome the rate-controlling step (i.e. the oxygen and electrode transfers) in the redox reaction VO_2^+/VO^{2+}.

3.2 Electrochemical properties

Cyclic voltammetry experiments at different scan rates were carried out to investigate electrochemical behavior of prepared felt electrodes towards VO^{2+}/VO_2^+ redox couples. The electrochemical behavior improvement of these samples was evaluated through four parameters, described as follow: i) current density values for oxidation and reduction peaks as well as ratio of oxidation and reduction current density peaks ($I_{pa,}$ I_{pc}) and ii) onset potential for oxidation process ; iii) the ratio of oxidation and reduction peak current densities (*Ipa/Ipc*, closed to 1 for reversible one electron process); iv) peak potential (E_a, E_c) and peak-to-peak potential separation (ΔEp=59 mV for reversible one electron process) [30].

Figure 7 illustrates the 10th cycle of the CV curves, which well-defined peaks for both oxidation and reduction processes can be appreciated in all as-prepared electrodes. Comparing all electrodes, the oxidation and reduction peaks current density values of the as-prepared electrodes are increasing in the following order (in parenthesis the I_{pa} and I_{pc} values

obtained from the voltammograms of the Figure 7): HT (I_{pa} =12.5, I_{pc} = 6.7 mA/cm^2) << HTW (I_{pa}=22.9, I_{pc} = 15.6 mA/cm^2) < HTN (I_{pa} = 27.4, $I_{pc=}$ 16.1 mA/cm^2) < HTNW electrode (I_{pa}=29.7, I_{pc} = 22.6 mA/cm^2). The low current density collected by the pristine electrode (i.e. HT) indicates a poor electrocatalytic activity towards the VO^{2+}/VO_2^+ reaction. Moreover, the onset oxidation potential found was the highest than that of all samples (ca. 0.30 V vs Hg/Hg_2SO_4). An improved electrocatalytic activity (i.e. higher I_{pc} and I_{pc} values as well as lower onset potential) displayed the HTW electrode as consequence of the WO_3-functionalities. These functionalities could be beneficial for the activation of electron and oxygen transfer processes towards the VO^{2+}/VO_2^+ reaction. Significant increase of current density as well as lower onset potential (ca. 0.26 V vs Hg/Hg_2SO_4) can be appreciated in the HTN electrode due to the incorporation of the nitrogen functionalities. These N-functionalities offers one lone pair of electron to effectively donor, which could facilitate the electron transfer as well as the adsorption of vanadium [31, 32, 33]. The simultaneous presence of WO3 and N-functionalities enhanced the electrocatalytic activity towards the positive half-cell reaction leading to the highest current density performed and lower onset potential (ca. 0.23 V vs Hg/Hg_2SO_4).

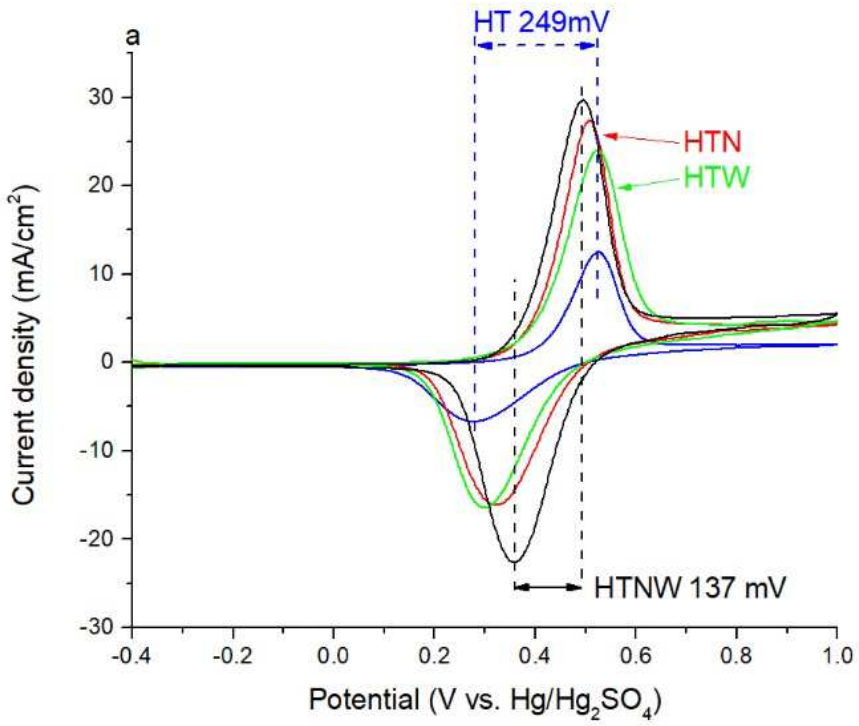

Figure 7 CV diagrams of as-prepared electrodes in 0.05M $VOSO_4$/1M H_2SO_4 solution at the scan rate of 1mV/s

The same trend was found with the *Ipa/Ipc* and ΔE_p values. The value of *Ipa/Ipc* for the HTNW electrode is very close to ca.1.2, which is lower value than HTW (~1.7), HTN (~1.6) and HT (~1.8) electrodes and the peak-to-peak separation potential (ΔE_p) value is HTNW (137 mV) whereas for the other samples are HTN (186 mV), HTW (230), and HT (249 mV). The combination of these features, suggests the potential synergistic effect due to the simultaneous modification of the HT electrode by WO_3 and N groups. These functionalities lead to remarkable higher electrocatalytic activity (i.e. higher reversibility and current density collected) for the positive half-cell reaction than HTW, HTN and HT electrodes.

The mass-transfer features for as-prepared electrode have been assessed using Randles-Secvic equation. Figure 8 despites the linear – relationship of the peak current densities values for oxidation and reduction process as a function of square root of the scan rate. In all as-prepared electrodes, peak currents densities are proved to be nearly proportional to the square root in the whole range of scan rates investigated, thus revealing that process is unequivocally controlled by the diffusion of the species in solution. In addition, the slope of the HTNW electrode was higher for both, oxidation and reduction processes, comparing with all electrodes studied, suggesting the improved mass-transfer reaction. The improved mass-transfer reaction on HTNW electrode can be ascribed to the highest electrochemically surface area due to the combination of WO_3 and N functionalities.

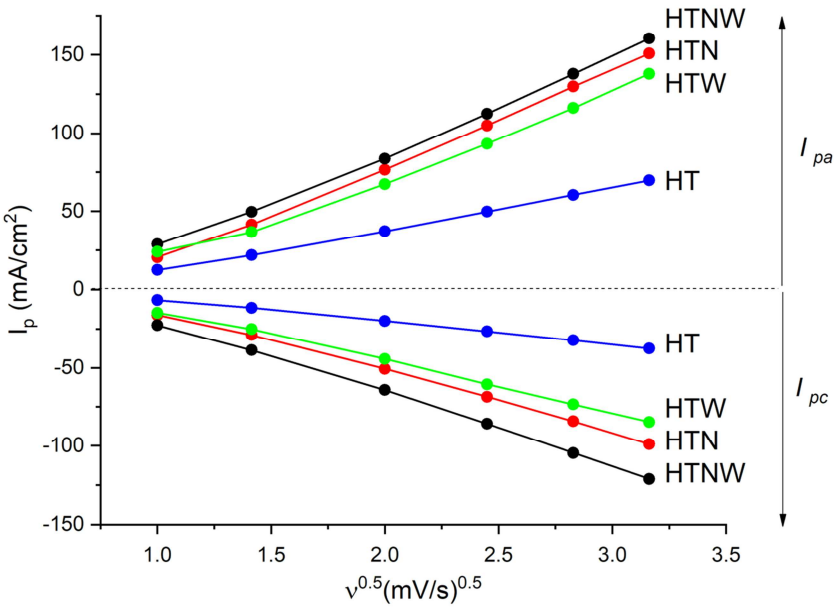

Figure 8. Linear-relationship plot between the anodic and cathodic current density peaks vs scan rates.

Electrochemical impedance spectroscopy (EIS) data support our claims, as shown in Figure 7. In all as-prepared electrodes, a straight line at low frequencies and a semi-circle at high frequencies are the components of the Nyquist impedance plot obtained, suggesting that the reaction of VO^{2+} /VO_2^{+} is a mixture of charge transfer and diffusion-controlled processes. Consequently, the equivalent circuit shown in the inset of Figure 9 simulates the classical Randles circuit for the aforementioned mixed control electrochemical process. The following elements can be appreciate in the equivalent circuit: 1) the R_s element represents the bulk electrolyte resistance; 2) R_{ct} denotes charge transfer resistance occurred at the interface of electrode material and electrolyte solution; 3) CPE-1 is ascribed to constant phase element, which is related to the double-layer capacitance of the interface between electrode and electrolyte, and 4) CPE-2 element represents the diffusion capacitance in pores of the electrodes. The parameters obtained after the fitting data are listed in Table 1 for less than 10% error.

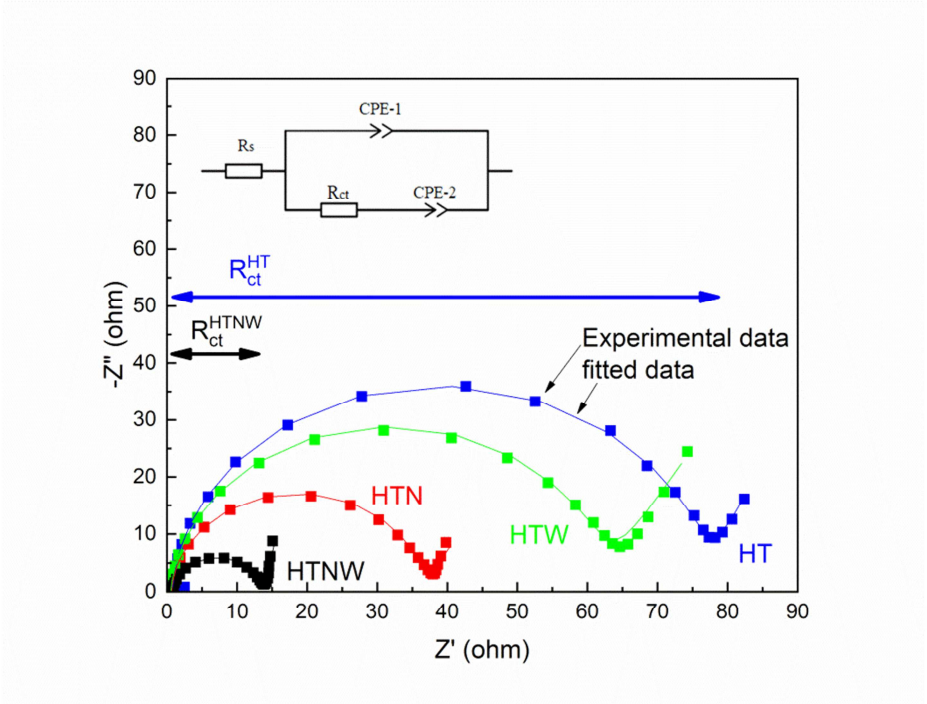

Figure 9. Nyquist impedance plots of the different carbon felt electrodes in a 0.05 M $VOSO_4$/1.0 M H_2SO_4 solution at open-circuit potential.

No significant changes can be appreciated by the R_s values for all samples, indicating that the poor influence of the treatment in the electrical properties of the electrodes. However, the charge-transfer resistance (R_{ct}) at the electrode/electrolyte interface is strongly influenced by the treatment. Comparing all electrodes, a significant decrement of the R_{ct} can be observed in the following order (resistance values are given in parenthesis): HT (75.62 Ω) > HTW (57.66 Ω) > HTN (34.88 Ω) >> HTNW (12.4 Ω), indicating a faster electron transfer rate on the surface of HTNW electrode. The same trends are evidenced for Y_1 and Y_2 values. The Y_1 and Y_2 values obtained for HTNW electrode were significantly the highest of all electrodes tested, indicating that the combination of N-and WO_3 -containing groups enhances the electric double-layer capacitance of electrode/solution interface as well as diffusion capacitance. Thus, the HTNW electrode favors the electron transfer process and facilitate the absorption and the diffusion of vanadium ions in the pores of the electrode leading to higher electrocatalytic effect, in accordance with the results obtained in CV analysis. These findings can be probably attributed to the synergistic effect of the N- and WO_3-functionalities that could be beneficial for boosting the performance of VRFB in the market.

Table 1. Parameters obtaining from fitting the Nyquits plots with the equivalent circuit model in inset of Figure 7

Sample	Rs (ohm)	CPE-1		Rct (ohm)	CPE-2	
		Y_1	n_1		Y_2	n_2
HT	0.75791	0.00193	0.96142	76.18	0.38637	0.76209
HTN	0.66482	0.00166	0.96764	35.89	0.73095	0.69781
HTW	0.54717	0.00165	0.9526	61.6	0.25353	0.68545
HTNW	0.78787	0.00489	0.9393	13	2.36	0.87898

3.3 Capacity and power features in VRFB flow cell

All these characteristics remark that the simultaneous modification of the treated carbon felt by WO_3 and N-heteroatoms has a synergetic effect, creating higher surface area (i.e. highly number of active sites) as well as facilitating the electron and oxygen transfer processes towards the VO^{2+} /VO_2^+ reaction (i.e. lower charge transfer resistance values). Thus, the higher active site density and the faster kinetics envisage the well-performance at higher current densities without higher voltage losses. Consequently, these electrodes constitute a clear alternative for increasing the power density capability and clearly could decrease the cost of the stack.

Figure 10 displays the voltage profile for both processes, charge and discharge, employing the as-prepared electrodes (HTNW or HTW or HTN or HTN) as positive electrode and HT as negative electrode in galvanostatic mode at 200 mA/cm^2. The HTNW shows remarkably larger discharge capacity in comparison with all as-prepared electrodes, attaining values up to 492 mAh. Notably, the electrolyte utilization ratio (EU%) achieved was 51% for the HTNW electrode (theoretical capacity values of the electrolytes is 965 mAh). Furthermore, a drastically decrement of the voltage drop was observed for HTNW electrode for both processes, in comparison with HTN, HTW and HT electrode, indicating lower polarization. For example, the IR-drop values obtained using HT, HTW and HTN electrodes was around 700 mV, significantly higher than HTNW electrode (i.e. 550 mV) due to the enhanced electrocatalytic activity. These findings are consistent with the voltage efficiency obtained for all electrodes, depicted in Figure 10. Particularly, it is remarkable the increment of the VE using HTNW electrode in comparison with all electrodes, attaining values up to 70%. Besides, the columbic efficiency yields up to 98%@200 mAcm^{-2}, arising values of the EE up to 70 %.

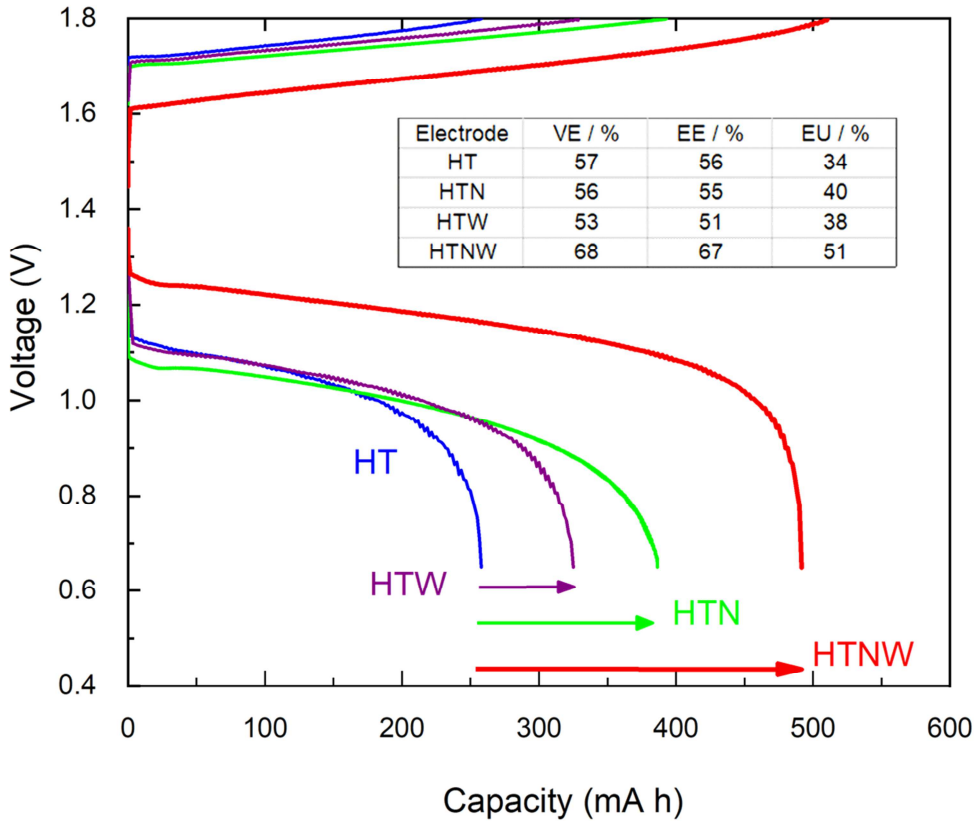

Figure 10. Comparison of the electrochemical performance for all as prepared electrodes, showing the voltage

Materials	Electrolyte	Current density/ (mA/cm^2)	CE / %	VE / %	EE / %	Electrolyte utilization / %	ref
WO_3-hydrothermal	1M $VOSO_4$ + 3M H_2SO_4	70	99	78.9	78.1	41	[14]
		80	99.9	76.7	76.6		
		90	99.5	75.1	74.7		

profiles for charge and discharge process at 200 mA cm^{-2}.

For better understanding, the Table 2 shows a comparison of the performance in terms of efficiency and electrolyte utilization ratio carried out for the WO_3-based electrodes found in the literature.

		100	99.8	72.2	72.0		
WO_3/SAC	1.5 M $VOSO_4$ + 3M H_2SO_4	50	94.5	85.2	80.5	70	[13]
WO_3/ Nanowire/ Graphene/foam	1.6 M $VOSO_4$ + 2.5M H_2SO_4	40	90.7	92.3	83.7	63	[34]
		80	95.0	83.7	79.5	66	
		120	96.2	75.9	73.0	39	
		160	98.2	68.8	67.6	20*	
Nb-Doped Hexagonal WO_3	1.6 M $VOSO_4$ + 2.5M H_2SO_4	40	92.4	92.1	85.1	15	[18]
		80	93.2	83.8	78.1	13	
		120	95.1	75.0	71.3	9	
		160	95.3	69.1	65.8	4*	
Nitrogen-tungsten oxide	1.8 M $VOSO_4$ + 3M H_2SO_4	200	96.3	67.9	65.4	51	This work

Table 2 Comparison of electrolyte, different efficiencies and electrolyte utilization percent of previously reported WO_3-based electrode materials

*Values calculated from the reference

In order to evaluate the performance of the VRFB for power-related application using HTNW electrodes, the peak power values determination has been evaluated. Figure 11 shows the characteristic polarization curves obtained for VRFB using both electrodes, HT and HTNW. Significantly differences can be appreciated in the performance originated by the following voltage losses: 1) kinetic activation of electrode in the range of 0 to 100mA cm^{-2}, 2) iR losses or ohmic resistance in the range of 100 to 400 $mAcm^{-2}$, associated with the contact resistant of all components, ionic resistance and electrical resistance in electrodes, and 3) transport-losses in the range of 425 to 500 $mAcm^{-2}$ due to concentration for polarization, where a mass transfer-limiting currents appears, associated with bulk reagent delivery to the electrode.

Comparing each region for both VFRB batteries and taking into account that the all elements are the same with the exception of positive electrode; the following features can be draw: 1) HT electrode originates greatly dramatic voltage drop, raising a kinetics more favorable in VRFB using HTNW electrode; 2) using HT electrodes lead to poor electrocatalytic activity than HTNW electrode in accordance with the VE trend; 3) The limiting current values are 200 and 400 mA cm^{-2} for HT and HTNW electrodes, respectively, which indicates substantial improvement mass-transport limitation of the HTNW electrodes, leading to the HTNW

electrode offers higher surface area available for electron and oxygen transfer electrode; 4) increment of the power peak up to more than 2-fold using HTNW electrode (i.e. power peak value of the 350 mWcm-2) in comparison with HT electrode (i.e. power peak values 150 mWcm-2).

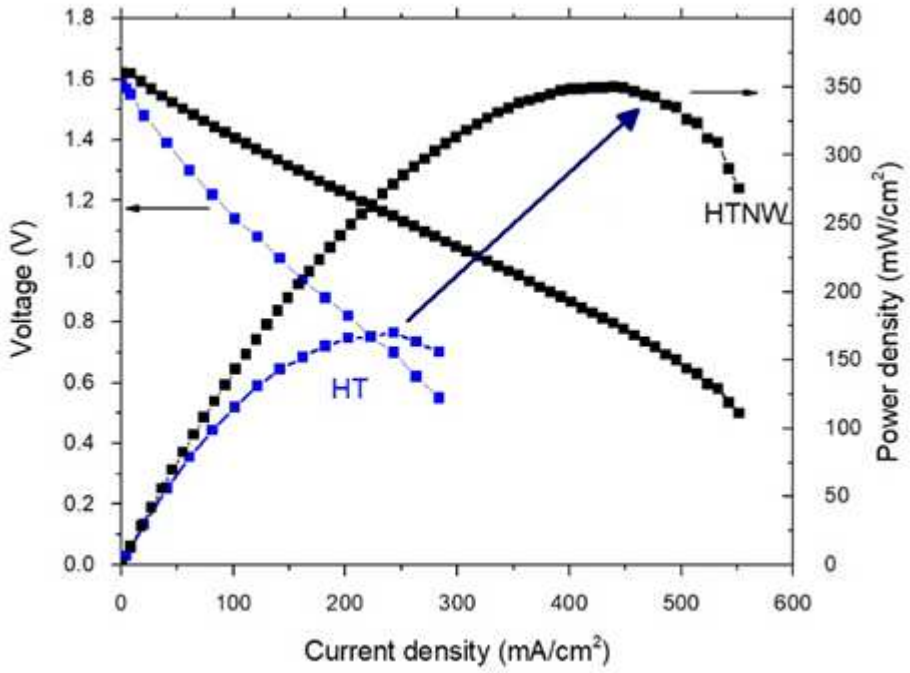

Figure 11. Polarization curves and measured power density for HT and HTNW electrode

4. Conclusion

In summary, a Nitrogen and WO3-functionalities have been successfully implemented on the surface of carbon felt by low-cost, easy scalable and environmentally-friendly hydrothermal method. The combination of the aforementioned functionalities exhibit a higher electro catalytic activities (i.e. reversibility and high current density) than individual activity of the electrocatalyst, promoting high electron and oxygen transfer rate as well as mass-transfer diffusion features. In particular, the charge transfer resistance at the interface electrode and electrolyte is dramatically decreased from 75.62 to 12.4 Ω for HT and HTNW electrode, respectively. In addition, the HTNW electrode demonstrate outstanding performance as positive electrode in VRFB. The feasibility of high-capacity values at high current density applied (200 $mAcm^{-2}$) has been demonstrated, achieving an electrolyte utilization ratio of the 51% and energy efficiency values up to 70%. Finally, more than 2-fold enhanced power

density can be easily achieved for the VRFB using HTNW electrode in comparison with HT electrode, allowing to decrement of the stack size as well as cost of the battery.

Acknowledgement

Authors thank Generalitat de Catalunya for financial support through the CERCA Program, MINECO for additional support by coordinated project ENE2016-80788-C5-5-R and Fundación Ramón Areces funding through BAT-LIMET project. S.M.L. for his Juan de la Cierva, Formación fellowship (FJCI-2014-19745). S.M.L. thanks MINECO for his Juan de la Cierva – Formación fellowship (FJCI-2014-19745).

Author contributions:

S.M. prepared the electrodes and carried out the characterization of electrodes by FE-SEM; XRD, Raman, ATR-FTIR and electrochemical experiments. S.M.L has contributed in the synthesis and characterization of the samples. M.G.H reported on the data interpretation; CF, TA and J.R.M. interpreted all data discussion and arguments. C.F. and J.R.M. led the research. All authors participated to the article preparation.

References.

1. Darling, R.M., et al., *Pathways to low-cost electrochemical energy storage: a comparison of aqueous and nonaqueous flow batteries.* Energy & Environmental Science, 2014. **7**(11): p. 3459-3477.
2. Sun, B. and M. Skyllas-Kazacos, *Chemical modification of graphite electrode materials for vanadium redox flow battery application—part II. Acid treatments.* Electrochimica Acta, 1992. **37**(13): p. 2459-2465.
3. Sun, B. and M. Skyllas-Kazacos, *Modification of graphite electrode materials for vanadium redox flow battery application—I. Thermal treatment.* Electrochimica Acta, 1992. **37**(7): p. 1253-1260.
4. Jin, J., et al., *Identifying the active site in nitrogen-doped graphene for the VO2+/VO2+ redox reaction.* ACS nano, 2013. **7**(6): p. 4764-4773.
5. Huang, R.-H., et al., *Investigation of active electrodes modified with platinum/multiwalled carbon nanotube for vanadium redox flow battery.* Journal of the Electrochemical Society, 2012. **159**(10): p. A1579-A1586.
6. Flox, C., et al., *Active nano-CuPt 3 electrocatalyst supported on graphene for enhancing reactions at the cathode in all-vanadium redox flow batteries.* Carbon, 2012. **50**(6): p. 2372-2374.
7. Cai, Y., et al., *Graphene nanosheets-tungsten oxides composite for supercapacitor electrode.* Ceramics International, 2014. **40**(3): p. 4109-4116.
8. Huang, Y., et al., *N, O Co-doped carbon felt for high-performance all-vanadium redox flow battery.* International Journal of Hydrogen Energy, 2016.
9. Wang, W. and X. Wang, *Investigation of Ir-modified carbon felt as the positive electrode of an all-vanadium redox flow battery.* Electrochimica Acta, 2007. **52**(24): p. 6755-6762.
10. Li, B., et al., *Bismuth nanoparticle decorating graphite felt as a high-performance electrode for an all-vanadium redox flow battery.* Nano letters, 2013. **13**(3): p. 1330-1335.

11. He, Z., et al., *Mn 3 O 4 anchored on carbon nanotubes as an electrode reaction catalyst of V (IV)/V (V) couple for vanadium redox flow batteries.* Electrochimica Acta, 2015. **176**: p. 1434-1440.
12. Ejigu, A., M. Edwards, and D.A. Walsh, *Synergistic Catalyst–Support Interactions in a Graphene–Mn3O4 Electrocatalyst for Vanadium Redox Flow Batteries.* ACS Catalysis, 2015. **5**(12): p. 7122-7130.
13. Yao, C., et al., *Carbon paper coated with supported tungsten trioxide as novel electrode for all-vanadium flow battery.* Journal of Power Sources, 2012. **218**: p. 455-461.
14. Shen, Y., et al., *Electrochemical catalytic activity of tungsten trioxide-modified graphite felt toward VO 2+/VO 2+ redox reaction.* Electrochimica Acta, 2014. **132**: p. 37-41.
15. Vázquez□Galván, J., et al., *Hydrogen□Treated Rutile TiO2 Shell in Graphite□Core Structure as a Negative Electrode for High□Performance Vanadium Redox Flow Batteries.* ChemSusChem, 2017. **10**(9): p. 2089-2098.
16. Zhou, H., et al., *CeO 2 decorated graphite felt as a high-performance electrode for vanadium redox flow batteries.* RSC Advances, 2014. **4**(106): p. 61912-61918.
17. Wu, X., et al., *PbO 2-modified graphite felt as the positive electrode for an all-vanadium redox flow battery.* Journal of Power Sources, 2014. **250**: p. 274-278.
18. Kabtamu, D.M., et al., *Electrocatalytic activity of Nb-doped hexagonal WO 3 nanowire-modified graphite felt as a positive electrode for vanadium redox flow batteries.* Journal of Materials Chemistry A, 2016. **4**(29): p. 11472-11480.
19. Mayrhuber, I., et al., *Laser-perforated carbon paper electrodes for improved mass-transport in high power density vanadium redox flow batteries.* Journal of Power Sources, 2014. **260**: p. 251-258.
20. Liu, Q., et al., *High performance vanadium redox flow batteries with optimized electrode configuration and membrane selection.* Journal of The Electrochemical Society, 2012. **159**(8): p. A1246-A1252.
21. Sun, L., et al., *Nitrogen-doped graphene with high nitrogen level via a one-step hydrothermal reaction of graphene oxide with urea for superior capacitive energy storage.* Rsc Advances, 2012. **2**(10): p. 4498-4506.
22. Liu, H., et al., *An electrochemically activated graphite electrode with excellent kinetics for electrode processes of V (II)/V (III) and V (IV)/V (V) couples in a vanadium redox flow battery.* RSC Advances, 2014. **4**(98): p. 55666-55670.
23. Li, M. and J. Xue, *Integrated synthesis of nitrogen-doped mesoporous carbon from melamine resins with superior performance in supercapacitors.* The Journal of Physical Chemistry C, 2014. **118**(5): p. 2507-2517.
24. Schieder, M., et al., *Hierarchically porous tungsten oxide nanotubes with crystalline walls made of the metastable orthorhombic polymorph.* Journal of Materials Chemistry A, 2013. **1**(2): p. 381-387.
25. Cançado, L.G., et al., *Quantifying defects in graphene via Raman spectroscopy at different excitation energies.* Nano letters, 2011. **11**(8): p. 3190-3196.
26. Guo, B., et al., *Controllable N-doping of graphene.* Nano letters, 2010. **10**(12): p. 4975-4980.
27. Casanovas, J., et al., *Origin of the large N 1s binding energy in X-ray photoelectron spectra of calcined carbonaceous materials.* Journal of the American Chemical Society, 1996. **118**(34): p. 8071-8076.
28. Pels, J., et al., *Evolution of nitrogen functionalities in carbonaceous materials during pyrolysis.* Carbon, 1995. **33**(11): p. 1641-1653.
29. Sharifi, T., et al., *Formation of active sites for oxygen reduction reactions by transformation of nitrogen functionalities in nitrogen-doped carbon nanotubes.* ACS nano, 2012. **6**(10): p. 8904-8912.
30. Bard, A.J., et al., *Electrochemical methods: fundamentals and applications*. Vol. 2. 1980: Wiley New York.
31. Shao, Y., et al., *Nitrogen-doped mesoporous carbon for energy storage in vanadium redox flow batteries*. Journal Power Sources, 195, 13, 2010, 4375.
32. Flox, C et al., *Thermo–chemical treatments based on NH3/O2 for improved graphite-based fiber electrodes in vanadium redox flow batteries.* Carbon, 60, 2013, Pages 280-288

33. Park, M. et al., *Corn protein-derived nitrogen-doped carbon materials with oxygen-rich functional groups: a highly efficient electrocatalyst for all-vanadium redox flow batteries.* Energy Environ. Sci., *2014, 7,3727*
34. Kabtamu, D.M., et al., *Three-dimensional annealed WO 3 nanowire/graphene foam as an electrocatalytic material for all vanadium redox flow batteries.* Sustainable Energy & Fuels, 2017.

Supplementary Information

High-power vanadium redox flow batteries based on synergistic effect of N- and WO_3 decorated carbon felt in positive half-cell reaction

Mir Ghasem Hosseini [a, b*1], Seyedabolfazl Mousavihashemi [a, c], Sebastián Murcia-López [c], Cristina Flox [c, *2], Teresa Andreu [c], Joan Ramón Morante [c, d]

[a] Department of Physical Chemistry, Electrochemistry Research Laboratory, University of Tabriz, Tabriz, Iran

[b] Engineering Faculty, Department of Materials Science and Nanotechnology, Near East University, 99138, Nicosia, North Cyprus, Mersin 10, Turkey

[c] IREC, Catalonia Institute for Energy Research, Jardins de les Dones de Negre 1, Sant Adrià de Besós, 08930 (Spain)

[d] Facultat de Física, Universitat de Barcelona, C. Martí i Franqués, 1, 08028, Barcelona, Spain

[1] Corresponding author. Tel: +98 413 339 3138. E-mail: mg-hosseini@tabrizu.ac.ir
[2] Corresponding author. Tel: +34 933 562 615. E-mail: cflox@irec.cat

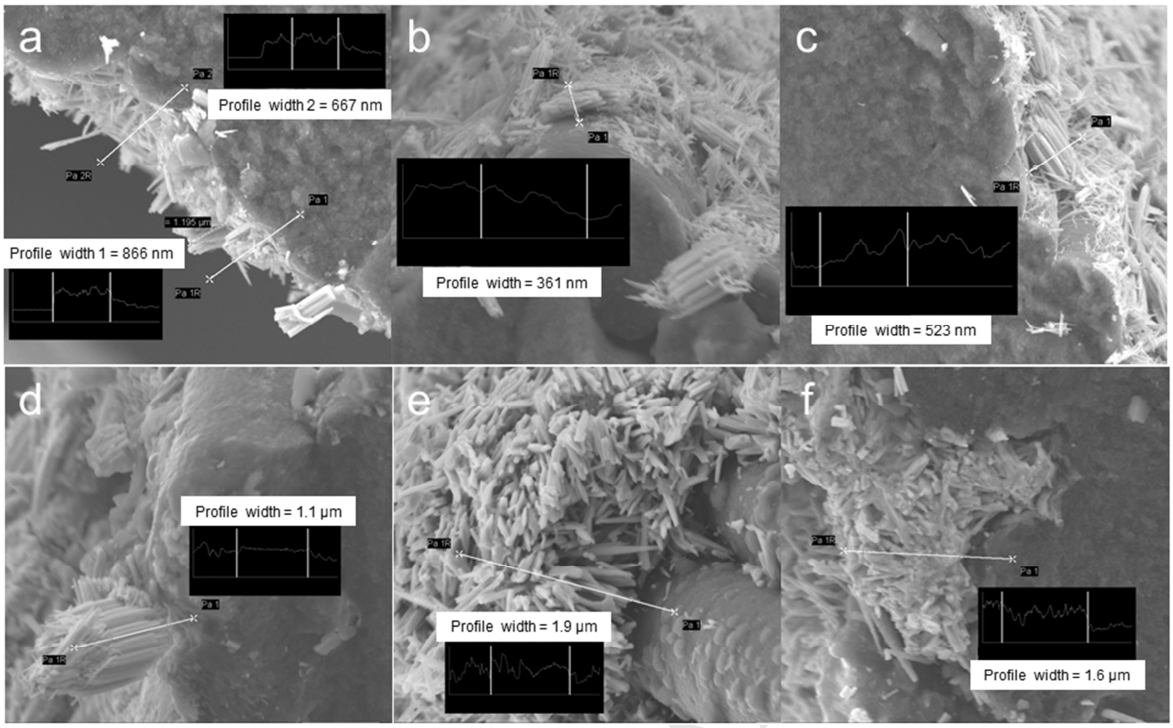

Figure S1. FE-SEM cross-section images of the HTW (a), (b), (c) and HTNW (d), (e), (f) electrodes.

Table S1 elemental contents of prepared samples determined by EDS

	C	O	N	W
HT	100	0	0	0
HTN	69.22	9.96	20.82	0
HTW	18.7	60	0	21.3
HTNW	4.59	65.84	4.67	24.9

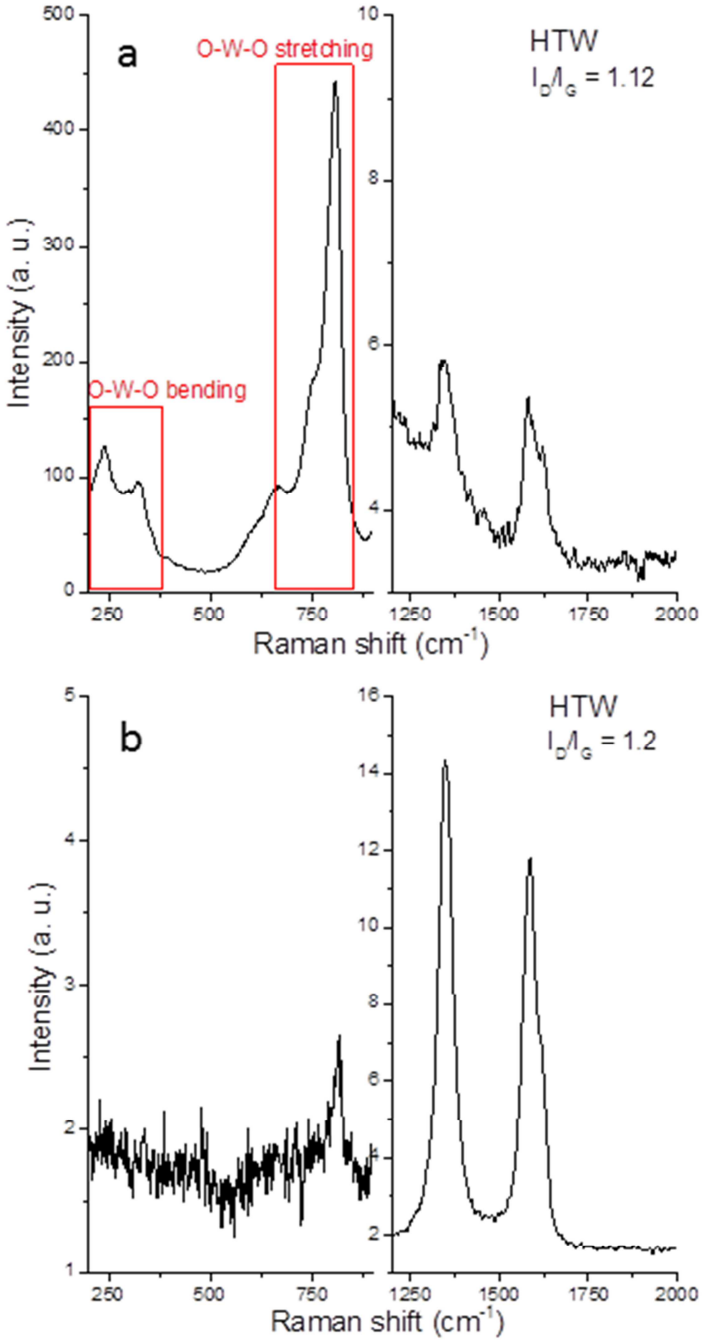

Figure S2. I_D/I_G ratio obtained in WO3 (a); and Felt (b) - related peaks on the HTW sample